ALEKSIJ AKSIMENTIEV*), ROBERT HOŁYST**)

Application of the Euler characteristic to the study of homopolymer blends and copolymer melts

Summary — The Euler characteristic is applied to study the phase separation/ordering phenomena occurring in polymer mixtures. Several methods used to compute Euler characteristics are described and discussed in terms of accuracy and efficiency. A novel, robust and exact algorithm based on simplex decomposition is presented. The simulated morphology of spinodal decomposition and the phase equilibrium diagram of gradient copolymers are analyzed in terms of Euler characteristics. Again, the Euler characteristics are applied to specify the connectivity of bicontinuous patterns, to distinguish the disperse and the bicontinuous morphologies, and to detect the percolation transition. During the spinodal decomposition, the dynamic transformation between the bicontinuous and the droplet patterns is shown to involve the formation of a transient "cylindrical" morphology.
Key words: spinodal decomposition, phase separation, Euler characteristic, homopolymer blends, gradient copolymers, morphology.

Morphology is a ubiquitous feature of any multicomponent system: any spatial variation of a local property (*e.g.*, concentration) can be treated as a complex geometrical object and viewed by drawing isosurfaces. Also, any process of phase separation or ordering can be treated as a time-dependent morphological transformation. For example, if a homogeneous binary mixture (*AB*) is quenched to reach the unstable part of its miscibility gap, the domains rich in component *A* or *B* will be formed shortly after the quench [1]. In the case of a symmetric mixture, a single bicontinuous interface is formed (Fig. 1a). The domains grow on average with time, while their connectivity decreases. In the case of a strongly asymmetric mixture disconnected droplets are formed at the very beginning of the phase-separation process (Fig. 1b). As the average size of the domains increases, the number of droplets decreases, and their sha-

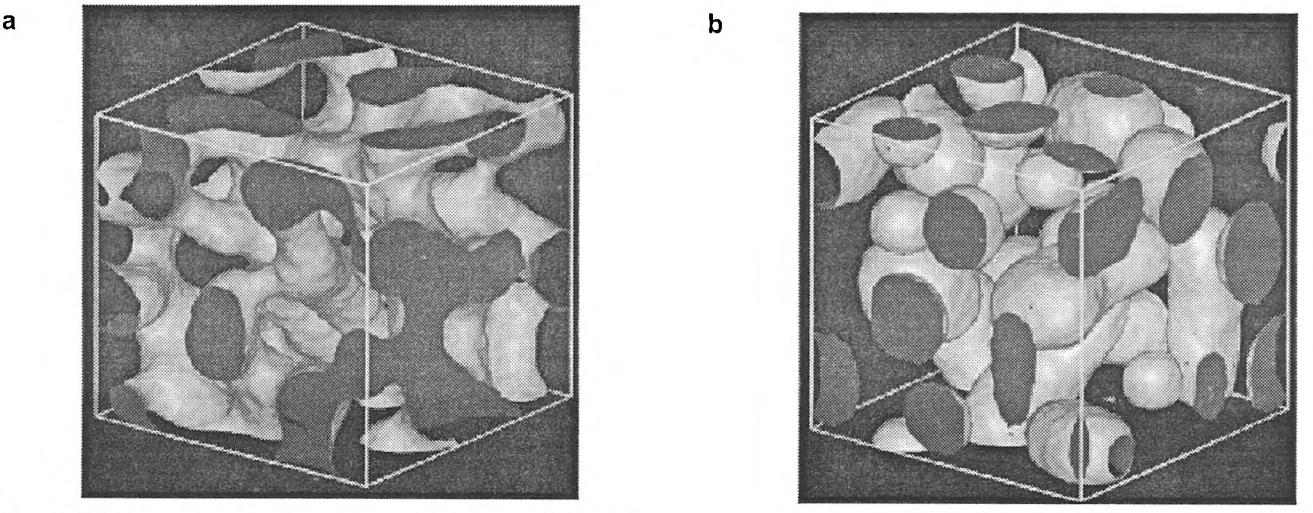

Fig. 1. The bicontinuous (a) and droplet (b) morphologies

*) Material Science Laboratory, Mitsui Chemicals, Inc., 580-32 Nagaura, Sodegaura-City, Chiba 299-0265, Japan.
**) Institute of Physical Chemistry and College of Science, Polish Academy of Sciences, Kasprzaka 44/52, 01-224 Warsaw, Poland.

pes become more and more spherical with time. Remarkably, under some specific quench conditions, the bicontinuous can be dynamically transformed into the droplet morphology, *i.e.*, at a certain intermediate stage of the phase separation process. These phase separation phenomena, observable in any immiscible mixture, are of extreme importance for the polymer industry, especially that the most common technological process in which two polymers are combined into a single material, is extrusion, *i.e.*, a process of extensive mechanical mixing run at high temperatures. The strong incompatibility of different polymer species, causes that, during the extrusion process, mixing occurs only rarely on the molecular scale. After extrusion, the blend is rapidly cooled to below the glass transition or crystallization temperature. In high polymers the processes of phase separation and coalescence are very slow so that the resulting material will preserve the morphology developed on its being processed and even on further treatment involving, *e.g.*, press molding. The properties of the resulting composite will combine the properties of the raw materials in the proportion determined by blend morphology and the properties of the interface itself.

Other examples of morphological transformations include order-disorder and order-order phase transitions in complex mixtures such as block copolymer melts. An *A*—*B* diblock copolymer is a polymer consisting of a sequence of *A*-type monomers chemically joined to a sequence of *B*-type monomers. Even a small degree of incompatibility (difference in interactions) between monomers *A* and monomers *B* can induce phase transitions. However, an *A*-homopolymer and a *B*-homopolymer are chemically joined in a diblock, and therefore a system of diblocks cannot undergo a microscopic phase separation. Instead, a number of order-disorder phase transitions take place in the system between the isotropic phase and spatially ordered phases in which *A*-rich and *B*-rich domains, of the size of a diblock copolymer, are periodically arranged into lamellar, hexagonal, bcc, and double gyroid structures. The covalent bond joining the blocks rests at the interface between the *A*-rich and B-rich domains.

At the mesoscopic level of description, a Landau-Ginzburg model of phase transitions in diblock copolymer systems has been formulated by Leibler [2] and later refined by Fredrickson *et al.* [3]. Matsen *et al.* [4—6] have used the self-consistent field theory to describe phase transitions in such systems. For $f = 0.5$ (f — volume fraction of *A*-monomers in the system) only the lamellar phase (LAM) is stable within a periodic stack of flat interfaces (Fig. 2a). As f is decreased, the double gyroid phase (DG) appears (Fig. 2b). This phase consists of two

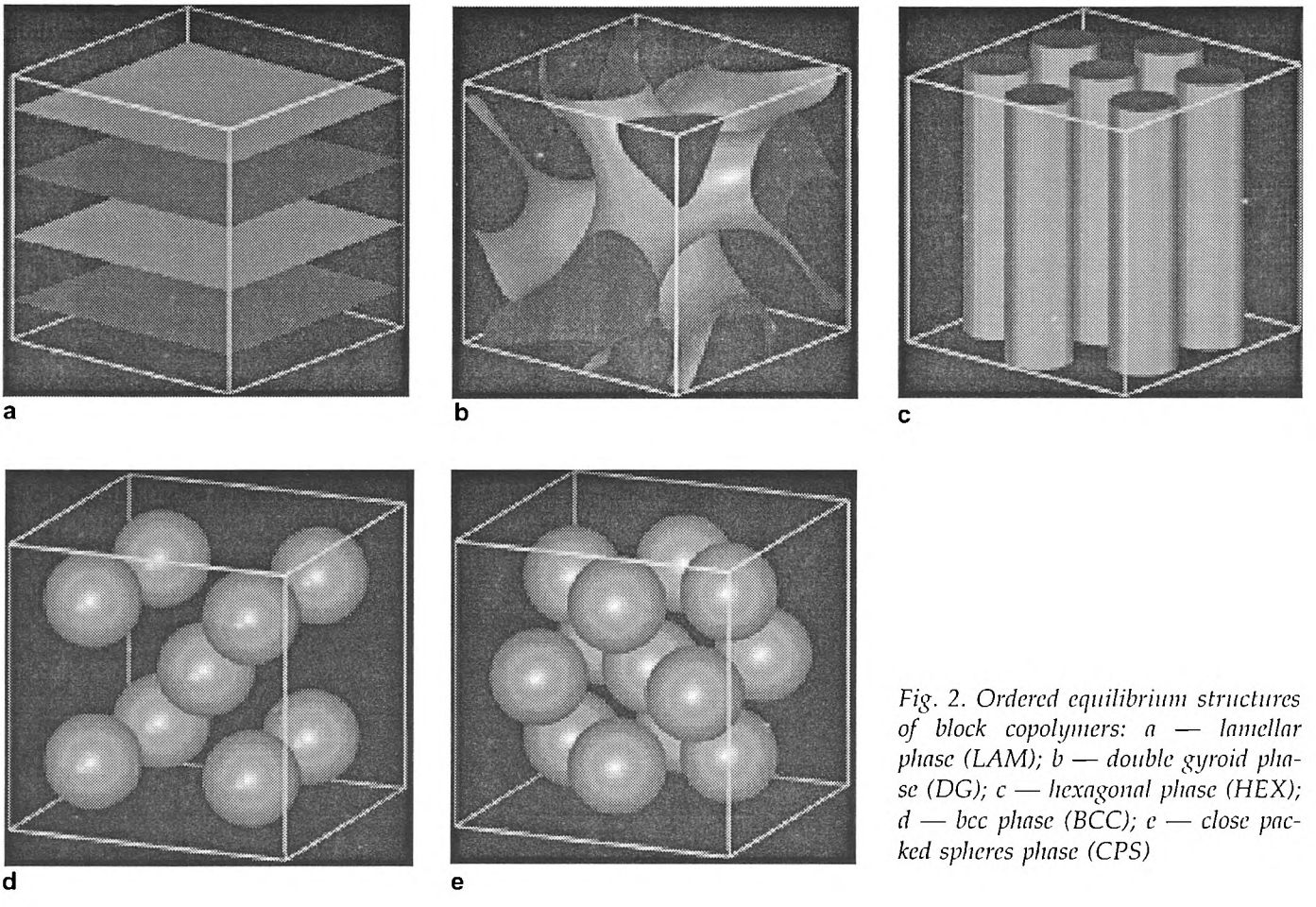

Fig. 2. Ordered equilibrium structures of block copolymers: a — lamellar phase (LAM); b — double gyroid phase (DG); c — hexagonal phase (HEX); d — bcc phase (BCC); e — close packed spheres phase (CPS)

gyroid surfaces within a unit cell. They form boundaries between the *A*-rich and the *B*-rich domains. The symmetry of the phase is Ia$\bar{3}$d [7] and each surface has genus 5 per unit cell [7, 8]. As a next step, a transition to the hexagonal phase (HEX) and *bcc* phase occurs (Figs. 2c and 2d). In the hexagonal phase, a minority component forms cylinders arranged on the hexagonal lattice and inserted into the matrix of the majority component. In the *bcc* phase (symmetry Im$\bar{3}$m), the minority component forms spheres arranged on the *bcc* lattice and surrounded by the majority component. The last phase which appears in the system is the close packed spheres (CPS) phase which consists of the spheres of the minority phase arranged either on the *fcc* or *hcp* lattice (Fig. 2e). The theoretical studies on the system have been greatly stimulated by experiments. The cylindrical, spherical and lamellar phases have been known for a long time [9], but only recently novel bicontinuous structures have been discovered in the diblock copolymer systems [10—13]. The originally discovered bicontinuous ordered structure has been misidentified in the TEM experiments [13]; later this structure has been shown to be the double gyroid phase [14] (Fig. 2b). In addition to the equilibrium phases, a number of complex metastable morphologies have been observed in the vicinity of the HEX-DG-LAM phase transition lines, *e.g.*, the hexagonally modulated lamellae of hexagonally perforated layers (the catenoid phase) shown in Figs. 3a and 3b, respectively. Those phases, which are metastable phases, could last for a long time owing to the very slow kinetics of phase transformation and large energy barriers caused by topological defects. The number of possible morphologies in block copolymers is infinite; already in the triblock copolymers, many new morphologies have been found to occur [15, 16].

In the past, studies on such morphological transformations were hampered by the lack of adequate experimental tools and theoretical methods. Recent advances in experimental techniques, including Laser Scanning Confocal Microscopy (LSCM) [17, 18] and Transmission Electron Micro-Tomography (TEMT) [19], have made it possible to visualize directly the interface in 3D polymer systems, to measure the surface area and to obtain curvature distributions. The obvious advantage of the full morphological description over conventional scattering data is the information it gives about the interface topology. A quantity that describes the surface topology is the genus, g, and the Euler characteristic, $\chi_{Euler} = 2(1 - g)$. The genus has a very simple interpretation: for a closed surface, this is the number of holes in the surface. Thus, for a sphere $g = 0$ ($\chi_{Euler} = 2$), for a torus $g = 1$ ($\chi_{Euler} = 0$), and for a pretzel $g = 2$ ($\chi_{Euler} = -2$). A large and negative Euler characteristic indicates a highly interconnected, bicontinuous morphology. In contrast, a disconnected droplet morphology is characterized by a large positive Euler characteristic, because the Euler characteristic of a system of disconnected surfaces is equal to the sum of the Euler characteristics for the individual

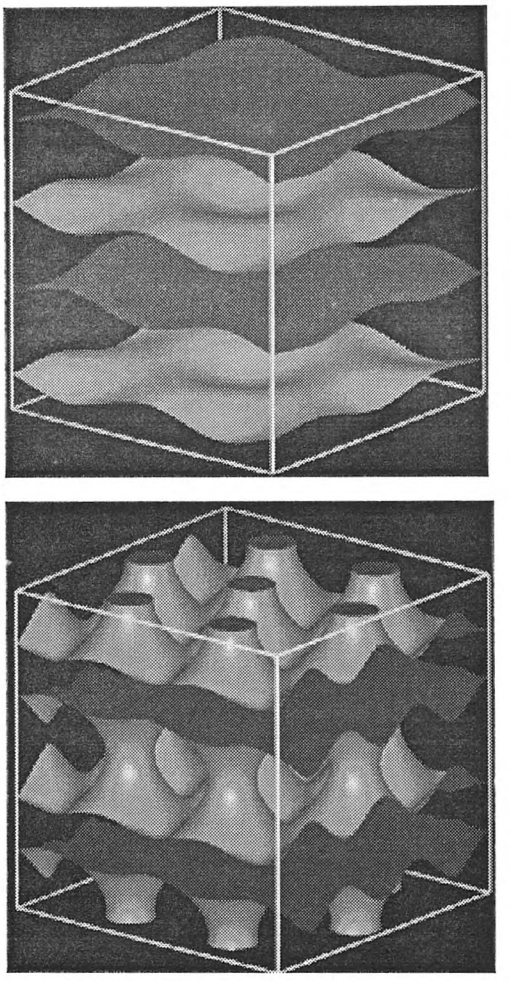

Fig. 3. Ordered metastable phases of block copolymers: a — hexagonally modulated lamellae (HML); b — hexagonally perforated layers (catenoid phase) (HPL)

surface. Thus, the calculated Euler characteristic allows to characterize the type and complexity of patterns. Also, the Euler characteristic facilitates the study of percolation problems, because the crossover between the positive and negative Euler characteristic signifies percolation. The Euler characteristic density determines the mechanical properties of a composite material, diffusion transport, and current conductivity. Moreover, in the three-dimensional systems comprising disconnected objects (such as in Fig. 1b), the Euler characteristic is useful in estimating the number of separate objects without actually separating the objects. A similar reasoning can be applied to any complex three-dimensional object. Examples of complex morphologies include porous materials, zeolites, composite materials, biological tissues, and irregular spatial-temporal patterns occurring, *e.g.*, in chemical reaction-diffusion systems. Summing up, by computing the Euler characteristic of the interface, the domain connectivity can be characterized quantitatively in an unambiguous way, which provides a valuable information about system morphology, almost undetectable from traditional scattering data or 2D micrographs. This paper sets out to present methods for

computing the Euler characteristic and to exemplify their applications.

METHODS FOR COMPUTING THE EULER CHARACTERISTIC

The Euler characteristic is usually calculated by using the Gauss-Bonnet theorem [20—24] or by the Euler formula [25—27]. The Gauss—Bonnet theorem relates the Euler characteristic, χ_{Euler}, of a closed surface to the local Gaussian curvatures $K(\mathbf{r})$:

$$\chi_{Euler} = \frac{1}{2\pi}\int_S K(\mathbf{r})dS \tag{1}$$

where the integral is taken over the surface. A number of different schemes have been proposed to calculate the local curvatures and the integral in Eq. (1).

Direct discretization of the derivatives

For a surface described by an analytical expression

$$\phi(x, y, z) = 0 \tag{2}$$

the integral (1) can be evaluated analytically, at least so in principle. The Gaussian curvature at point $\mathbf{r}$ is given as

$$K(\mathbf{r}) = \frac{1}{2}\{-(\partial_i n_i)^2 + [\nabla n(\mathbf{r})]^2\} \tag{3}$$

where $n(\mathbf{r})$ is the unit normal vector at point $\mathbf{r}$ given by the gradient of the field $\phi(\mathbf{r})$,

$$n(\mathbf{r}) = \frac{\nabla\phi(\mathbf{r})}{|\phi(\mathbf{r})|} \tag{4}$$

For numerical calculations the following formulas are used [25]:

$$K = \frac{1}{\phi_x^2 + \phi_y^2 + \phi_z^2}\cdot\frac{C}{A} \tag{5}$$

where A and C are given by

$$A = -(\phi_x^2 + \phi_y^2 + \phi_z^2) \tag{6}$$

$$C = \phi_x^2(\phi_{yz}^2 - \phi_{yy}\phi_{zz}) + \phi_y^2(\phi_{xz}^2 - \phi_{xx}\phi_{zz}) + \phi_z^2(\phi_{xy}^2 - \phi_{xx}\phi_{yy}) + 2\phi_x\phi_z(\phi_{xz}\phi_{yy} - \phi_{xy}\phi_{yz}) + 2\phi_x\phi_y(\phi_{xy}\phi_{zz} - \phi_{xz}\phi_{yz}) + 2\phi_y\phi_z(\phi_{yz}\phi_{xx} - \phi_{xy}\phi_{xz}) \tag{7}$$

The simplest way to calculate the Euler characteristic is to disregard the surface integral in Eq. (1) and to calculate the average Gaussian curvature

$$\langle K\rangle = \frac{\int_S K(\mathbf{r})dS}{\int_S dS} \tag{8}$$

by summing up the local curvature and dividing by the sum over the number of sampling points. Then the Euler characteristic is

$$\chi_{Euler} = \frac{1}{2\pi}\langle K\rangle S \tag{9}$$

where S *is the total surface area.*

In this case, calculation of the Euler characteristic reduces to the evaluation of the surface integral by the Monte-Carlo method. In a more elaborate approach, a certain surface area is assigned to each sampling point before the surface integral in Eq. (1) is evaluated numerically.

While affording a reasonably good accuracy for analytically well-defined surfaces, this scheme of calculation is very inaccurate if the field ϕ is specified by a discrete set of values (the lattice scalar field). In this case the surface is located between the lattice sites of different signs. The first, second and mixed derivatives can be evaluated numerically by using some finite difference schemes, which normally results in poor accuracy for discrete lattices. In addition, triangulation of the surface is required to compute the integral in Eq. (1) or to calculate the total surface area S. This procedure renders the method rather inefficient on a lattice as compared with other methods.

Method based on the first and second fundamental forms of differential geometry

In this method the local Gaussian curvatures are calculated by using the first and the second fundamental forms of differential geometry [20]. The surface is parameterized near the point of interest (POI) as $\mathbf{p}(u, v)$ (Fig. 4). The coordinates (u, v) are set arbitrarily on the surface

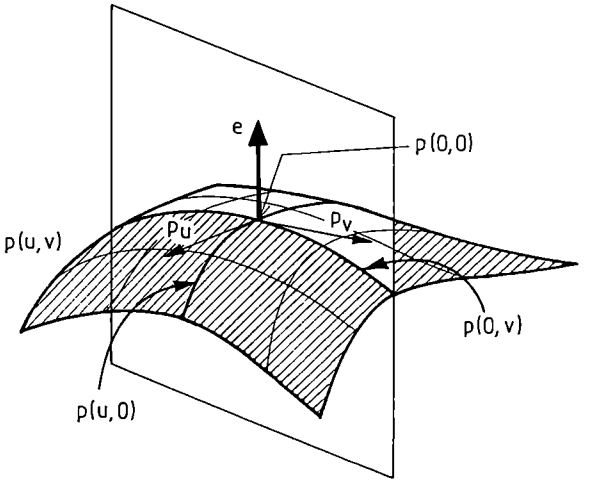

Fig. 4. A schematic diagram of the surface expressed in parametric form $\mathbf{p}(u, v)$ *and a "sectioning plane", which is comprised of* $\mathbf{e}$ *and* $\mathbf{p}(0, v)$; $\mathbf{p}(0, 0)$ *is the point of interest at which the local curvatures are determined [20]*

so as to locate POI at $\mathbf{p}(u, v) = (0, 0)$. The first and the second forms of differential geometry are expressed as

$$I = E\,du\,du + 2F\,du\,dv + G\,dv\,dv \tag{10}$$

and

$$H = L\,du\,du + 2M\,du\,dv + N\,dv\,dv \tag{11}$$

where *parameters E, F, G, L, M and N are related to the partial derivatives of the local parametric equation of the surface:*

$$E = \mathbf{p}_u \cdot \mathbf{p}_u, \quad F = \mathbf{p}_u \cdot \mathbf{p}_v, \quad G = \mathbf{p}_v \cdot \mathbf{p}_v,$$
$$L = \mathbf{p}_{uu} \cdot \mathbf{e}, \quad M = \mathbf{p}_{uv} \cdot \mathbf{e}, \quad N = \mathbf{p}_{vv} \cdot \mathbf{e} \tag{12}$$

Here $\mathbf{e}$ *is the unit vector normal to the surface at the POI defined by* $\mathbf{e} = p_u \cdot p_v / |p_u \cdot p_v|$ *and subscripts of* p *denote the partial derivatives.*

The mean H and Gaussian K curvatures are expressed as

$$H = \frac{EN + GL - 2FM}{2(EG - F^2)}$$
$$K = \frac{LN - M^2}{EG - F^2} \tag{13}$$

The surface is first "sectioned" by the plane that contains $\mathbf{p}_u$ and $\mathbf{e}$. The intersection between the plane and the surface is defined as $\mathbf{p}(u, 0)$. Parameters E and L are determined from $\mathbf{p}(u, 0)$. Then the surface is cut by the second plane which is defined by $\mathbf{p}(0, v)$. Now F, G and N can be computed. By eliminating M from Eqs. (12) and (13) the following expression is obtained:

$$f(i, K, H) \equiv 0 = 4F_i^2 \{L_i N_i - K(E_i G_i - F_i^2)\} + \\ - \{E_i N_i + G_i L_i - 2H(E_i G_i - f_i^2)\}^2 \tag{14}$$

where *subscript i denotes the ith set of the curvilinear coordinates.*

The local Gaussian curvature is determined by nonlinear regression fits performed after a number of sections at a given point has been made (this corresponds to different sets of local coordinates (u, v)). The Euler characteristic is then calculated as described above.

In principle, this method is more accurate than the direct derivative discretization method, since the derivative calculations are repeated several times at the same surface point. Nevertheless, the method gives only an approximate value of the Euler characteristic and the triangulation procedure cannot be avoided.

Parallel surface method

The parallel surface method has been developed to measure the interface curvature from 3D digital images [23]. A surface parallel to the interface is first formed by translating the original interface along its normal by an equal distance everywhere on the surface. The change in the surface area at an infinitely small parallel shift of the surface is

$$A(t) = A(0)\,(1 + 2\langle H\rangle t + \langle K\rangle t^2) \tag{15}$$

where t *is the displacement,* $\langle H\rangle$ *and* $\langle K\rangle$ *are the surface-averaged mean and Gaussian curvatures, and* $A(0)$ *and* $A(t)$ *are the total surface areas before and after the parallel shift.*

The Euler characteristic is given as

$$\chi_{Euler} = \frac{1}{2\pi}\langle K\rangle A \tag{16}$$

This method essentially requires triangulation of the surface and gives only an approximate value of χ_{Euler}. To increase the accuracy, a number of parallel shifts is usually made.

Digital pattern method

In the digital pattern method, an array of real data is transformed into the pixel pattern by using a thresholding procedure. Then the lattice is covered by black and white pixels. Local curvature variables are assigned to the corners of each black pixel [21] (Fig. 5). The Euler characteristic is given by the sum of the curvature variables over the boundary between black and white domains, which makes that method computationally very efficient. However, the loss of the information caused by the thresholding procedure leads to some specific situations when domain boundaries cannot be drawn unambiguously. Figure 6 presents one such case. The actual morphology of the interface is determined by the field values at the lattice sites. But after the thresholding procedure, the boundaries of the domain cannot be found. In two-dimensional systems, such ambiguous situations can be avoided by considering hexagonal pixels [22]. However, hexagonal pixels can be specified only for a specific type of simulations and cannot be easily designed and/or anticipated in experiments. In the 3D case, this problem can be solved in principle by covering the lattice with regular polyhedra other than cubes, but this is not very practical, since most simulations are carried out on a cubic lattice.

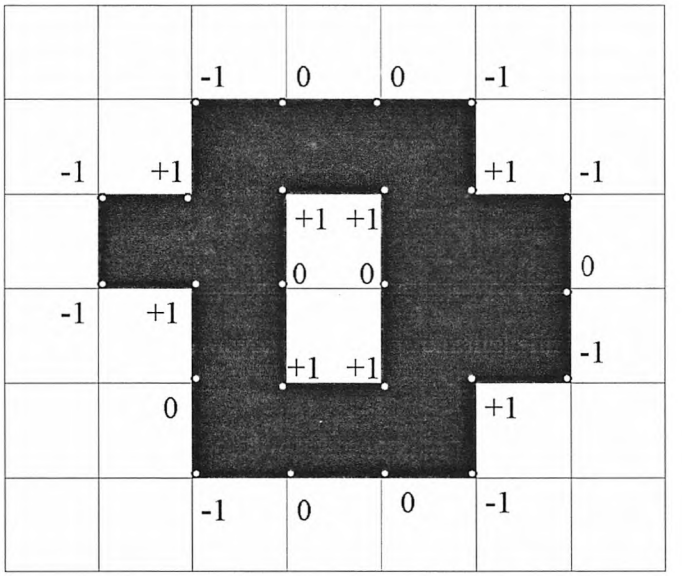

Fig. 5. The 2D illustration of the digital pattern analysis for computing the Euler characteristic. The local curvature variables $\tau \in \{-1, 0, +1\}$ *are assigned to each lattice site at the boundaries of black pixels. The Euler characteristic is the sum of local curvature variables* ($\chi = 8(+1) + 8(-1) + 8(0) = 0$)

Summarizing, the digital pattern method is computationally very efficient but, for cases similar to the one

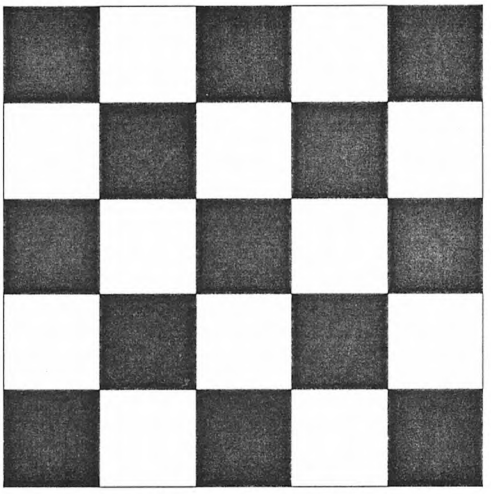

Fig. 6. An example when the Euler characteristic cannot be correctly determined by using the digital pattern analysis, because the boundaries of the domains after the thresholding procedure cannot be specified

shown in Fig. 6, it fails to calculate the Euler characteristic. Such cases are typical, however, when data are noisy or when the field values are distributed around the threshold value.

Techniques based on the Euler equation

Computation of the Euler characteristic based on Eq. (1) is not practical, particularly when the system is represented by a set of points on a lattice. A convenient way to compute χ_{Euler} is related to covering the surface with polygons. Calculation of the Euler characteristic is straightforward by using the Euler formula:

$$\chi_{Euler} = \#F + \#V - \#E \qquad (17)$$

where *#F, #V, and #E are the numbers of faces (#F), vertices (#V), and edges (#E) of all the polygons cut by the surface.*

Practically, this procedure is performed by decomposing the lattice into small subunits (simplexes). The surface inside each simplex is represented by simple polygons; the "local" Euler characteristic is calculated from the formula reported elsewhere (17). Since the Euler characteristic is an additive measure, the total Euler characteristic is obtained by summing up over all non-empty simplexes.

The most intuitive way to perform simplex decomposition of the lattice is to divide the lattice into small cubes [25]. The surface inside each small cube can be triangulated, *i.e.*, represented by interconnected triangles (*cf.* Fig. 7). As the most intuitive, the cube lattice decomposition scheme suffers from arbitrary choices. Thus, the six cases shown in Fig. 7 do not include all the possible cases and, when there are 6, 7, 8, 9, or 12 vertices in a small cube, the computation of the Euler characteristic leads to ambiguities, *viz.*, different connections between the points result in different values of the Euler

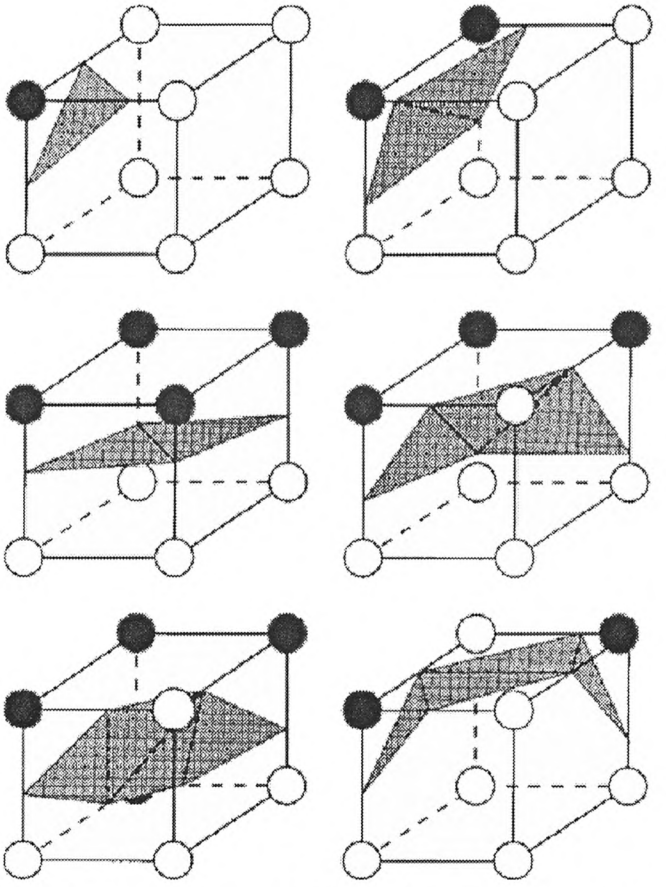

Fig. 7. Six cases of possible polygonal approximation for the isosurface inside a cube used in the cubic decomposition method [25, 26]

characteristic. Also, the more elaborate surface localization algorithm — the marching cube algorithm [28] — does not explore all the possibilities and, when field values are noisy, ambiguous situations can arise. An example is shown in Fig. 8 where, for a given field configuration, two different surface representations can be drawn. In case *a*, there are two surfaces inside the cube; in case *b*, the number of surfaces is 3. The two cases (Fig. 8) specify different numbers of connections between the triangles, a fact of immediate consequence on the Euler characteristic value. To resolve this problem, one can use the field values at the vertices of the cube to divide it further into smaller cubes, to find the field values at the vertices of the new cubes by interpolation, and to apply the surface approximation scheme again [16]. In such a way, the number of ambiguous situations can be significantly reduced, but not entirely eliminated.

An alternative way to avoid ambiguous surface approximations is to divide the original lattice into more primitive simplexes rather then into cubes. Each cube can be divided into six 5-vertex pyramids by introducing an additional point at the center of each cube. Now, the surface can be drawn unambiguously by using the pyramid classification scheme [29] (Fig. 9). Depending on the field values at the pyramid vertices and at the center of the four-vertex face, the surface is

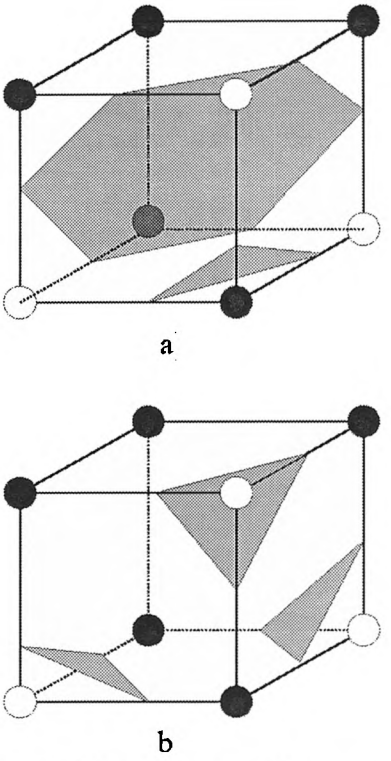

Fig. 8. The location of the intersections between the isosurface and the cube edges is the same in each Figure, (a) and (b), but the value of the Euler characteristic depends on the way the points are connected. This demonstrates the failure of the cubic decomposition method

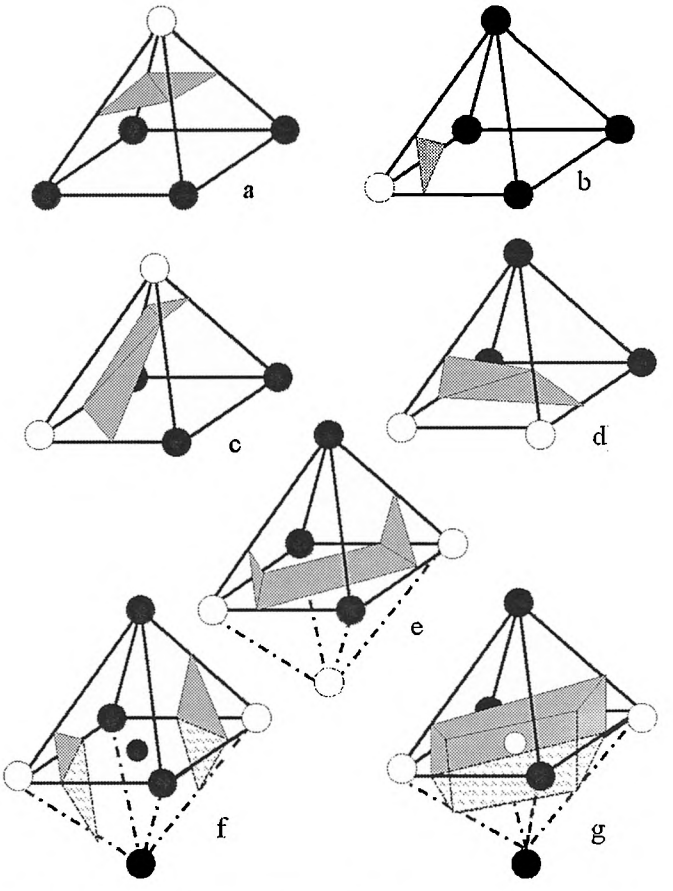

Fig. 9. Seven possible cases of the polygonal surface representation in a single pyramid. The Euler characteristic is calculated as a sum of the number of faces and the number of vertices reduced by the number of edges of the polygons. The black and white circles represents points with higher and lower values relative to the threshold value. The grey area is the schematic representation of the surface inside a pyramid [29]

represented by a triangle, tetragons, pentagons and hexagons. The case *e* in Fig. 9 can be further divided into two cases, similarly to the cases *f* and *g*, which modifies the way the surface is triangulated but with no consequence on the Euler characteristic. When Eq. (17) is used to compute the local Euler characteristic, one must keep in mind that some vertices, faces and edges are shared with the neighboring simplexes. Furthermore, to employ such a decomposition scheme, the field values at the center of the cube and at the centers of its faces should be found by linear interpolation. The use of interpolation for this purpose is justified, because the level of accuracy is the same as in the surface location procedure (also as a consequence of linear approximation).

A single lattice unit can also be divided into the simplest possible subunits, the primitive four-vertex pyramids. One possible realization of this procedure is shown in Fig. 10. Other decomposition schemes are also possible involving a single cube divided into 5 or 7 four-vertex pyramids [30, 31]. When the 4-vertex pyramid decomposition is employed, the surface inside the pyramid can be represented by only two cases: triangle or tetragon (Fig. 11). The combination of two neighboring 4-vertex pyramids can produce a single 5-vertex pyramid. However, the two cases shown in Fig. 11 cannot reproduce all the possible surface localizations defined within the 5-vertex decomposition scheme (*e.g.*,

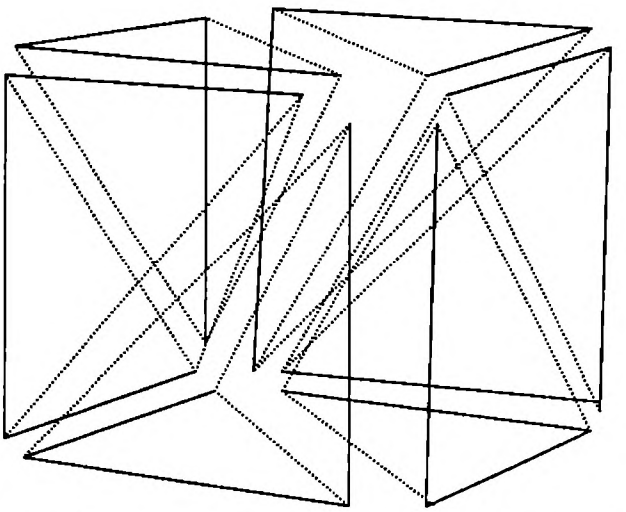

Fig. 10. The decomposition of a cubic lattice cell into six four-vertex pyramids

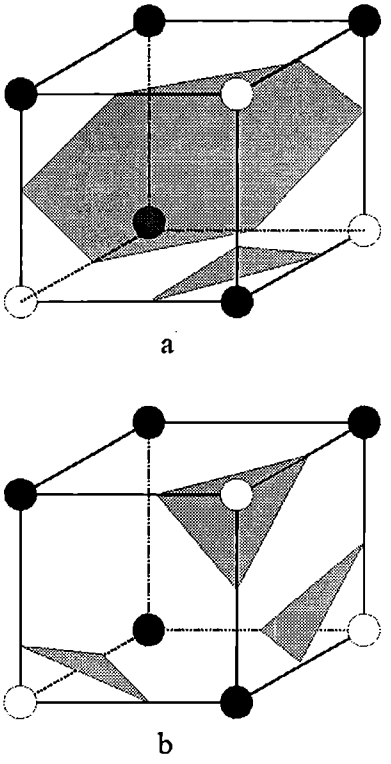

Fig. 8. The location of the intersections between the isosurface and the cube edges is the same in each Figure, (a) and (b), but the value of the Euler characteristic depends on the way the points are connected. This demonstrates the failure of the cubic decomposition method

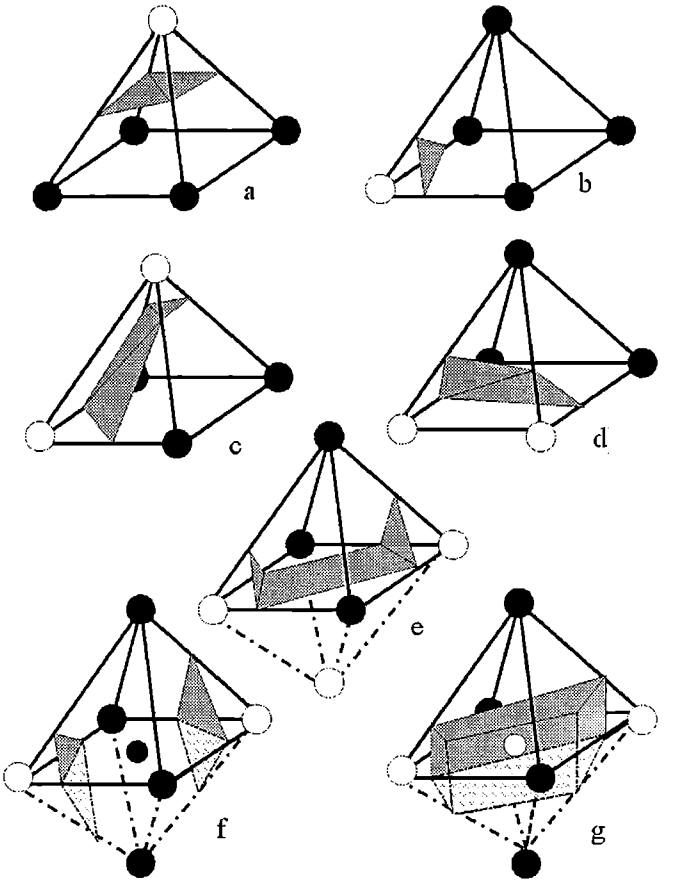

Fig. 9. Seven possible cases of the polygonal surface representation in a single pyramid. The Euler characteristic is calculated as a sum of the number of faces and the number of vertices reduced by the number of edges of the polygons. The black and white circles represents points with higher and lower values relative to the threshold value. The grey area is the schematic representation of the surface inside a pyramid [29]

represented by a triangle, tetragons, pentagons and hexagons. The case *e* in Fig. 9 can be further divided into two cases, similarly to the cases *f* and *g*, which modifies the way the surface is triangulated but with no consequence on the Euler characteristic. When Eq. (17) is used to compute the local Euler characteristic, one must keep in mind that some vertices, faces and edges are shared with the neighboring simplexes. Furthermore, to employ such a decomposition scheme, the field values at the center of the cube and at the centers of its faces should be found by linear interpolation. The use of interpolation for this purpose is justified, because the level of accuracy is the same as in the surface location procedure (also as a consequence of linear approximation).

A single lattice unit can also be divided into the simplest possible subunits, the primitive four-vertex pyramids. One possible realization of this procedure is shown in Fig. 10. Other decomposition schemes are also possible involving a single cube divided into 5 or 7 four-vertex pyramids [30, 31]. When the 4-vertex pyramid decomposition is employed, the surface inside the pyramid can be represented by only two cases: triangle or tetragon (Fig. 11). The combination of two neighboring 4-vertex pyramids can produce a single 5-vertex pyramid. However, the two cases shown in Fig. 11 cannot reproduce all the possible surface localizations defined within the 5-vertex decomposition scheme (*e.g.*,

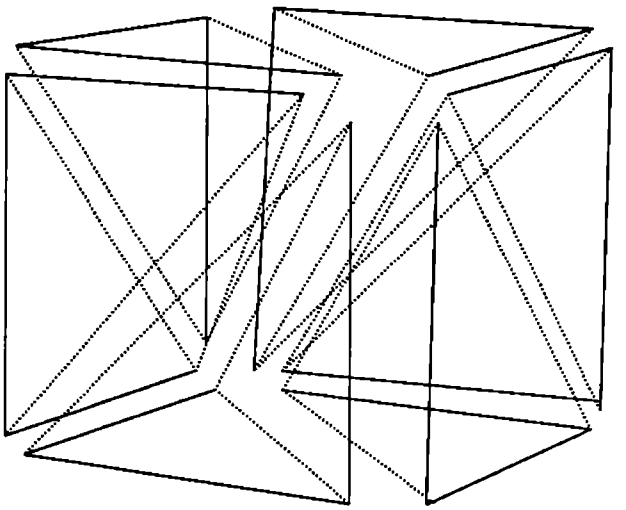

Fig. 10. The decomposition of a cubic lattice cell into six four-vertex pyramids

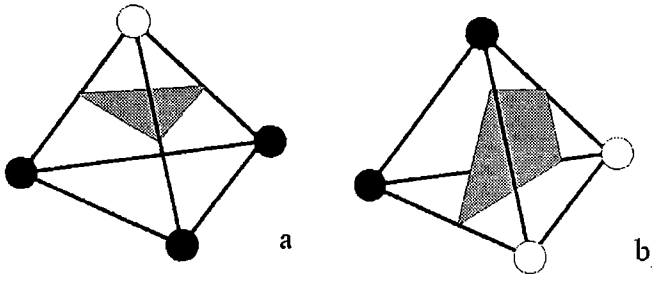

Fig. 11. Two possible cases of the polygonal surface representation in a single triangular pyramid. The black and white circles represent points with higher and lower values relative to the threshold value. The grey area is the schematic representation of the surface inside the pyramid

case *g*, Fig. 9). The choice of the decomposition scheme is dictated by the morphological measure that has to be calculated, the required speed of calculation, and by the available computational resources. Here, the 5- or 4-vertex pyramid decomposition can be applied to any irregular lattice and, therefore, is more general.

The best scheme for Euler characteristic calculations is the one that allows to consider the maximum number of possible connections within the same interpolation approximation. By using the 5-vertex simplex and 7 polygonal surface representations (Fig. 9) all the cases specified for the marching cube algorithm [28] and for the tetragonal simplex decomposition (Figs. 10, 11) can be reproduced. In addition, this decomposition scheme detects a few very specific surface configurations that cannot be reproduced within the other schemes. Therefore, we recommend using this scheme for a precise calculation of the Euler characteristic. Nevertheless, when the surface is smooth, *i.e.*, when more than one surface is very unlikely to be present in a single lattice cell, the 4-vertex scheme may be more practical due to its simplicity (especially when the surface has to be triangulated). In fact, triangulation of the surface is not required for the calculation of Euler characteristic; only the number of vertices, faces and edges is needed. That makes the calculations using the simplex decomposition scheme very efficient as compared with other methods.

EXAMPLES OF APPLICATION

Simulation of spinodal decomposition

The phase separation process of a binary *AB* polymer mixture has been investigated by computer simulations. We consider a homopolymer blend (*AB*) which consists of the molecules with the same indices of polymerization, N, and the same Kuhn segment lengths, σ. The average volume fraction of component *A* in the system is ϕ_0, and the state of the system is described by the local volume fraction of component *A*, $\phi(\mathbf{r})$, at all points r of the system. The phenomenological mesoscopic Langevin-type dynamic equation that relates a temporal change of $\phi(\mathbf{r})$ to a local current of component *A*, **J**, is simply a continuity equation [32]:

$$\frac{\partial\phi(\mathbf{r},t)}{\partial t} = -\nabla\mathbf{J} + \eta(\mathbf{r},t) \tag{18}$$

where *the stochastic term* $\eta(\mathbf{r}, t)$ *has been added in order to model the thermal noise in the system [1].*

At the limit of infinite viscosity, we can neglect the hydrodynamic flux contribution [33] $\phi(\mathbf{r})\mathbf{v}(\mathbf{r})$ to the local current **J** ($\mathbf{v}(\mathbf{r})$ is a local velocity). In this case, transport in the system is governed by the difference of chemical potentials, and one can postulate a linear relation between the local current and the gradient of the local chemical potential difference $\mu(\mathbf{r})$ [34, 35],

$$\mathbf{J}(\mathbf{r}) = -\int \frac{\Lambda(\mathbf{r}-\mathbf{r}')}{k_B T}\nabla'\mu(\mathbf{r}')d\mathbf{r} \tag{19}$$

The local chemical potential difference $\mu(\mathbf{r})$ is given by the functional derivative of a coarse-grained free energy functional $F(\phi)$,

$$\mu(\mathbf{r}) = \frac{\delta F[\phi]}{\delta\phi(\mathbf{r})} \tag{20}$$

The minimum length scale at which we shall describe the phase separation phenomena is about the size of a single polymer molecule. At this length scale, we can approximate the nonlocal Onsager coefficient $\Lambda(\mathbf{r} - \mathbf{r}')$ by the following expression [34]:

$$\Lambda(\mathbf{r} - \mathbf{r}') \cong ND\phi(1 - \phi)\,\delta(\mathbf{r} - \mathbf{r}') \tag{21}$$

where D *is the self-diffusion coefficient of polymer chains.*

Then we can take, consequently, the coarse-grained free energy functional $F[\phi]$ in the Flory-Huggins-de Gennes form:

$$F[\phi(\mathbf{r})] = \int d^3\mathbf{r}\left[f(\phi(\mathbf{r})) + \frac{\sigma^2}{36\phi(1-\phi)}(\nabla\phi(\mathbf{r}))^2 \right] \tag{22}$$

where f *is the usual Flory-Huggins free energy:*

$$f(\phi(\mathbf{r})) = \frac{1}{N}[\phi\ln(\phi) + (1 - \phi)\ln(1 - \phi)] + \chi_{Euler}\,\phi(1 - \phi)] \tag{23}$$

We introduce the following rescaled variables:

$$\mathbf{x} = \frac{(\chi - \chi_S)^{1/2}}{\sigma}\mathbf{r} \tag{24}$$

$$\tau = \frac{D(\chi - \chi_S)^2}{\chi_S\sigma^2}t \tag{25}$$

Here χ *is the Flory-Huggins interaction parameter,* $\chi_s = 1/(2N\phi_0(1 - \phi_0))$ *and* $\chi_{cr} = 2/N$ *are the values of* χ *at the spinodal and critical points, respectively.*

The time scale of the simulation is determined by the self-diffusion constant, D. It depends on system temperature and polymerization index as $\sim\mu_0 T/N^2$, where μ_0 is the microscopic monomeric mobility [32]. The final equation to be solved numerically is written in the rescaled variables as:

$$\frac{\partial\phi(\mathbf{x},\tau)}{\partial\tau} = \frac{1}{2\phi_0(1-\phi_0)}\nabla\left\{\phi(1-\phi)\nabla\left[\frac{\chi_{cr}}{2(\chi-\chi_{cr})}\cdot\ln\frac{\phi}{1-\phi} - \frac{2\chi\phi}{(\chi-\chi_{cr})} + \right.\right.$$
$$\left.\left. - \frac{1}{18\phi(1-\phi)}\nabla^2\phi + \frac{1-2\phi}{36\phi^2(1-\phi)^2}(\nabla\phi)^2\right]\right\} + \sqrt{\varepsilon}\zeta(\mathbf{x},\tau) \quad (26)$$

where the noise term $\zeta(\mathbf{x}, \tau)$ should satisfy the fluctuation-dissipation theorem (FDT),

$$\langle\zeta(\mathbf{x},\tau)\zeta(\mathbf{x}',\tau')\rangle = -\frac{1}{\phi_0(1-\phi_0)}\nabla\phi(1-\phi)\nabla\delta(\mathbf{x}-\mathbf{x}')\cdot\delta(\tau-\tau') \quad (27)$$

and the noise intensity $\varepsilon = \sqrt{\chi-\chi_s}$.

We solve Eq. (26) numerically on a cubic ($L^3 = 64^3$) lattice by using the first-order Euler scheme,

$$\phi(\bar{\mathbf{x}},\tau+\Delta\tau) = \phi(\bar{\mathbf{x}},\tau) + \Delta\tau\frac{\partial\phi(\bar{\mathbf{x}},\tau)}{\partial\tau} + \bar{\zeta}(\bar{\mathbf{x}}) \quad (28)$$

where $\bar{\mathbf{x}} = \Delta x[i, j, k]$, $i, j, k = 1, \ldots, L$ *is a position vector at the lattice,* Δx *is a lattice spacing (mesh size) and* $\Delta\tau$ *is a time step.*

Equation (28) contains the rescaled noise term $\bar{\zeta}(\bar{\mathbf{x}})$ written explicitly; this term has to be generated at each time step and each lattice site in accordance with the FDT, Eq. (27). To find the noise contribution to the change of the field configuration at time $\tau + \Delta\tau$, the field configuration at time τ is required, since the Onsager coefficient depends on local volume fractions, Eq. (21). To generate the noise in accordance with Eq. (27), we follow the ideas of Puri and Oono [36] and introduce an additional vector white noise $\vec{\xi}$ with the Gaussian components, which satisfies the following relation

$$\langle\xi_i(\mathbf{x},\tau)\xi_j(\mathbf{x}',\tau')\rangle = \frac{\phi(\mathbf{x})\,(1-\phi(\mathbf{x}))}{\phi_0(1-\phi_0)}\delta_{i,j}\delta(\mathbf{x}-\mathbf{x}')\delta(\tau-\tau') \quad (29)$$

If we now relate our noise variable ζ to ξ by

$$\zeta(\mathbf{x},\tau) = \nabla\bar{\xi}(\mathbf{x},\tau) \quad (30)$$

the FDT (27) will be satisfied. The white noise components are generated from the Gaussian distribution endowed with variance $\frac{\phi(\mathbf{x})\,(1-\phi(x))}{\phi_0(1-\phi_0)}$ independently at each lattice site. Finally, the noise contribution to discrete Eq. (28) is

$$\bar{\zeta} = \sqrt{\frac{\Delta\tau}{(\Delta x)^3}}(\chi-\chi_s)^{1/4}\xi \quad (31)$$

i.e., it is related to discretization [37, 38].

General features of the evolution of bicontinuous morphology

The simulated mixture was a polybutadiene—deuterated polybutadiene blend [39] (upper critical solution temperature, ~335 K). The starting conditions for simulations were generated by assigning the average-over-the-entire-system volume fraction of component *A* (ϕ_0) to each lattice point (ϕ_0 is conserved during the simulations). Morphology of the system can be characterized by the interface between the domains rich in com-

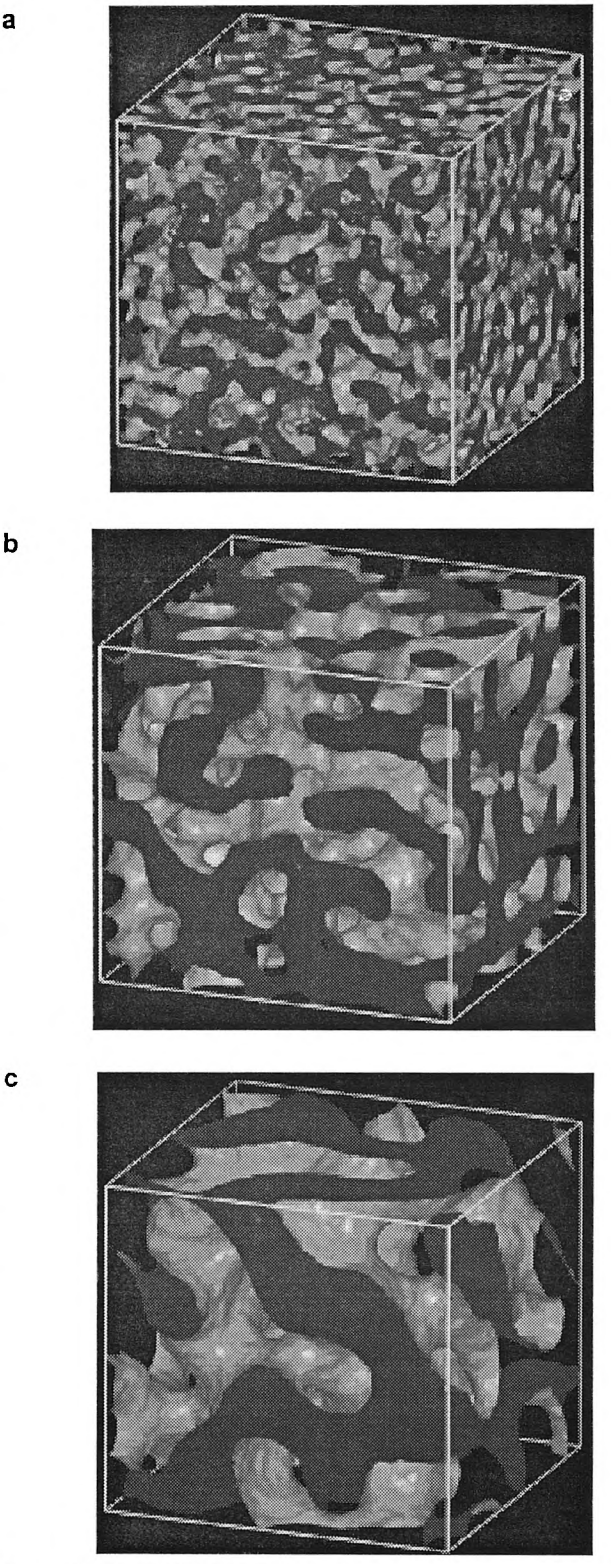

Fig. 12. Quantitative characterization of the phase-separated morphology of the symmetric mixture by computing the Euler characteristic. Different stages of the spinodal decomposition are shown in snapshots a—c; τ is the dimensionless time. The Euler characteristic is negative over the entire range of morphologies studied and indicates that the surfaces are bicontinuous. The Euler characteristic increases with dimensionless time. This indicates that the surface connectivity decreases. τ is: a) 6.23, b) 135.1, c) 1125; χ_{Euler} is: a) -4208, b) -428, c) -74

ponent A or component B. The interface can be specified as the points where the field $\phi(\mathbf{r})$ is equal to the average volume fraction of component A. One of the described algorithms (Fig. 9), was applied to the field configurations produced by the simulations in order to characterize the morphology of the blend.

Figures 12a—c present highly interconnected surfaces obtained from a computer simulation, which represent different stages of phase separation in a binary polymer mixture (only one A-rich, phase is shown). The temperature of the simulated blend was set at 298 K and the average volume fraction equal to 0.5 (symmetric mixture). The data shown were obtained in the form of a three-dimensional scalar lattice field. The calculated values of the Euler characteristic, -4208, -428, -74 for Fig. 12a, b, c, respectively, are negative and increase as the dimensionless simulation time, τ, is increased. The changes of the Euler characteristic indicate here that the connectivity of the surface decreases but the blend morphology remains bicontinuous.

The systems undergoing phase transitions (like spinodal decomposition) often exhibit scaling phenomena [1], *i.e.*, the morphological pattern of the domains at earlier moments looks statistically similar to the pattern appearing at later moments apart from the global change of scale implied by the growth of $L(t)$ — the domain size. Quantitatively, it means that, for example, the correlation function of the order parameter (density, concentration, magnetization, *etc.*)

$$g(\mathbf{r}, t) = g(\mathbf{r}/L(t)) \tag{32}$$

where

$$L(t) \sim t^n \tag{33}$$

the characteristic length scale in the system, scales algebraically with time t with the exponent n varying with the universality class [1]. The Fourier transform of the correlation function gives the scattering intensity which can be represented by the following scaling form:

$$S(q, t) = L^d(t)Y(qL(t)) \tag{34}$$

where *q is the scattering wave-vector and Y is the scaling function.*

By assuming the scaling hypothesis, we can derive all the scaling laws for different morphological measures such as: the Euler characteristic $\chi_{Euler}(t)$, surface area $S(t)$, the distribution of the mean curvature $P(H, t)$ and of the Gaussian curvature $P(K, t)$. The scaling hypothesis implies the following scaling laws for any phase separating/ordering symmetric system irrespective of the universality class

$$\chi_{Euler}(t) \sim L(t)^{-3} \tag{35}$$

$$S(t) \sim L(t)^{-1} \tag{36}$$

$$P_H(H, t) \sim P_H^*(HL(t))/L(t) \tag{37}$$

$$P_K(K, t) \sim P_K^*(KL(t)^2)/L(t)^2 \tag{38}$$

The first law follows from the Gauss-Bonnet theorem, Eq. (1), relating the Gaussian curvature to the Euler characteristic. Since $K = 1/R_1R_2$, scaling implies $K \sim L(t)^{-2}$. In the symmetric system, the volume of one of the phases, $V \sim S(t)L(t)$ is fixed, therefore, $S(t) \sim 1/L(t)$, and the scaling (35) follows. These tests are robust, *i.e.*, they apply to any symmetric system exhibiting phase ordering/separating kinetics. The exponent n for the algebraic growth of $L(t)$ determines the behavior of all other quantities.

Our simulations confirmed that the scaling relations (32)—(36) hold at the late stages of the spinodal decomposition [39]. These results allow to predict the connectivity of the polymer matrix after a given time of phase separation without doing further simulations. However, scaling of local curvature distributions is largely affected by thermal undulations of the interface induced by the noise term [39]. The local curvature scaling is observed only if thermal motions of the interface have been smoothed out. Thus, during an LSCM measurement, thermal undulations are averaged out during the measurement time; in addition, the characteristic size of the thermal undulation is usually smaller than the microscope resolution. Therefore, the scaling (37), (38) can be experimentally observed [20].

Percolation transition and Euler characteristic

Figure 13a presents a highly interconnected surface obtained at the early moments of a computer simulation of the phase-separated polymer mixture (only one, A-rich, phase is shown). The temperature of the system and the average volume fraction were set at 298 K and equal to 0.35 (asymmetric blend), respectively. This field configuration was specified by a highly negative Euler characteristic, -3764. After a certain simulation time, the Euler characteristic became positive, 132 (Fig. 13b), which reflected the transformation of the bicontinuous into the dispersed morphology. This dispersed morphology continued to transform to decrease the number of droplets (Fig. 13c).

The possibility of forming droplets during the spinodal decomposition of a binary mixture depends on two factors: the average blend composition ϕ_0 and the depth of the temperature quench. It is convenient to regard the transformation from interconnected to disperse morphology as a percolation transition. The transformation is assumed to be described by considering only the geometrical features of the system, particularly by studying the minority domain volume fraction f_m. At some special value of f_m (at the percolation threshold value) the morphological transition occurs. It is important to distinguish the average A-component volume fraction (composition), ϕ_0, and f_m. The former quantity is a constant, whereas f_m can vary during the simulations. In the very long time limit f_m approaches the equilibrium value.

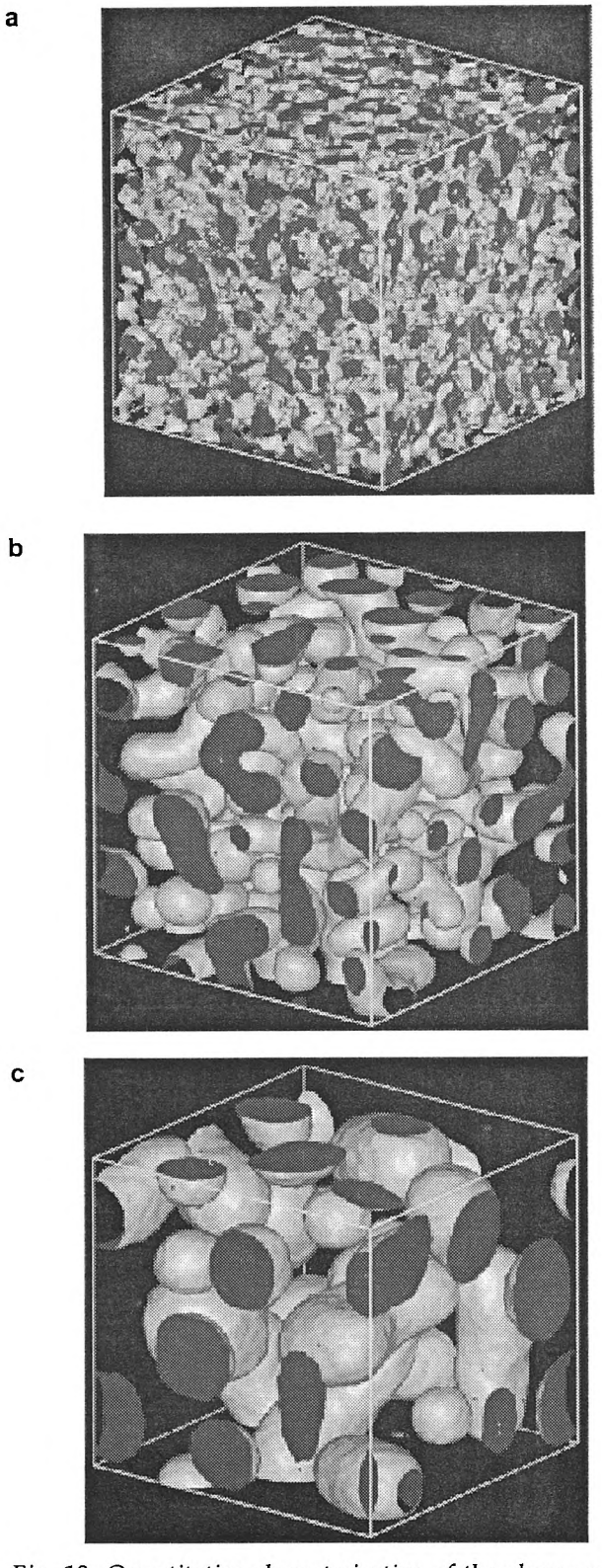

Fig. 13. Quantitative characterization of the phase-separated morphology of the asymmetric mixture by computing the Euler characteristic. Different stages of the spinodal decomposition are shown in snapshots a—c; τ is the dimensionless time. The Euler characteristic is initially negative and indicates that the morphology is bicontinuous. After a certain time the Euler characteristic becomes positive which indicates that the transition to the dispersed morphology has occurred. For dispersed morphology the Euler characteristic is equal to twice the droplet number; τ is: a) 1,88, b) 29.69, c) 274.25; χ_{Euler} is: a) -3764, b) +132, c) +36

$$f_m^{eq} = (\phi_0 - \phi_A^{(1)}) / (1 - 2\phi_A^{(1)}) \quad (39)$$

where $\phi_A^{(1)}$ *is the equilibrium volume fraction of component A in the minority phase (the symmetry of the phase diagram allows to consider only blends of* $\phi_0 \leq 0.5$*).*

The percolation assumption can be tested by calculating both the Euler characteristic and the minority domain volume fraction. Since the Euler characteristic is a direct measure of the domain connectivity, we identify the domain percolation at the point where the Euler characteristic attains zero.

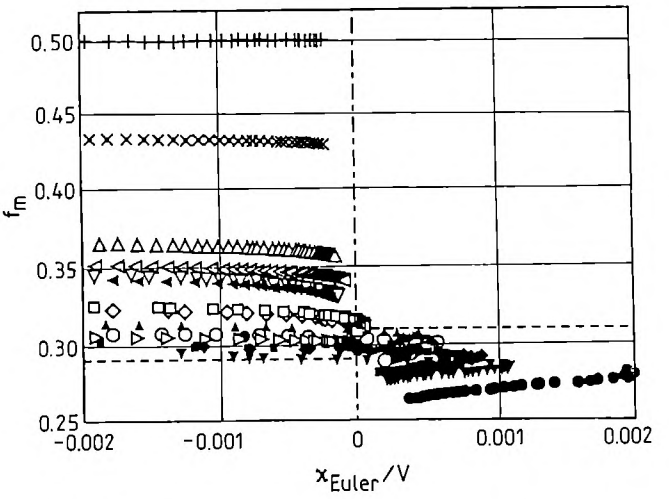

Fig. 14. The plot of the minority phase volume fraction, f_m, versus the Euler characteristic density for several simulation runs at different quench conditions, $f_m^{(eq)}$ = 0.225 ... 0.5. The bicontinuous morphology ($\chi_{Euler} < 0$) was not observed for $f_m < 0.29$, nor was the droplet morphology ($\chi_{Euler} > 0$) for $f_m > 0.31$. This observation suggests that percolation occurs at $f_m = 0.3 \pm 0.01$

In Fig. 14, the minority phase volume fraction, f_m, is plotted versus the Euler characteristic density for a large number of simulation runs performed under various quench conditions. For the symmetric blends ($\phi_0 = 0.5$), $f_m = 0.5$ and is independent of time and χ_{Euler}/V. For the asymmetric blends, f_m decreases with time and χ_{Euler}/V may change in sign. The bicontinuous morphology was not observed at $f_m < 0.29$, nor was the droplet morphology at $f_m > 0.31$. This observation suggests that percolation occurs at $f_m = 0.3 \pm 0.01$ and the percolation threshold is not very sensitive to the quench conditions.

Thus, one could expect to find a droplet morphology to occur at such quench conditions at which the equilibrium minority phase volume fraction (determined by the lever rule from the phase diagram) is lower than the percolation threshold. However, the time interval after which a disperse coarsening occurs would depend strongly on the quench conditions, because the volume fraction of the minority phase approaches the equilibrium value very slowly at late moments of a simulation.

Euler characteristic and morphological transformations in copolymer melts

The most intriguing property of block copolymer systems is their self-assemblying into well-defined ordered structures. The chemical architecture of copolymer chains together with the overall component compositions comprise the input parameters for mesoscopic models. The main aim of these models is to predict quantitatively the system morphology at equilibrium.

Consider a mixture of n polymer molecules in a volume V. Each molecule consists of N_A monomers of type A and N_B monomers of type B. Let $\{A\}$ and $\{B\}$ denote the positions of the monomers of type A and type B consequently in the chain. For example, in a chain $AABABAA$ the monomers occupy the following positions $\{A\} = \{1, 2, 4, 6, 7\}$ and $\{B\} = \{3, 5\}$. We assume all chains to be identical (we could also assume different sets $\{A\}$ and $\{B\}$ for each chain with the same averaged monomer distribution function). The location of the ith monomer in the αth molecule is given by the position vector $\mathbf{r}_i^\alpha$, and the orientation of the bond connecting monomers i and i - 1 is given by $\mathbf{u}_i^\alpha = \mathbf{r}_i^\alpha - \mathbf{r}_{i-1}^\alpha$. To describe a flexible polymer, the chain model is used, in which the monomers are described as being joined by freely rotating bonds of a fixed length l (we assume the same bond lengths for A—A, A—B and B—B bonds). The information that N monomers are connected to form a chain is specified by the spatial distribution function $W(\mathbf{r})$:

$$W(\mathbf{r}) = \prod_{i=1}^{N} \frac{\delta(|\mathbf{u}_i| - l)}{4\pi l_2} \tag{40}$$

where $\delta(x)$ *is the Dirac delta function, and* $N = N_A + N_B$ *is the index of polymerization.*

The interaction Hamiltonian with the specified short-range interactions between the monomers is given by the following expression [40, 41]:

$$H_I = \frac{\rho_0}{k_B T}\int \frac{d\mathbf{q}}{(2\pi)^3}\left[\frac{1}{2} w_{AA}\left|\hat{\phi}_A(\mathbf{q})\right|^2 + \frac{1}{2} w_{BB}\left|\hat{\phi}_B(\mathbf{q})\right|^2 + w_{AB}\hat{\phi}_A(\mathbf{q})\hat{\phi}_B(-\mathbf{q})\right] \tag{41}$$

where $\rho_0 = n(N_A + N_B)/V$ *is the number density of monomers in the system,* $\hat{\phi}_A(q)$ *and* $\hat{\phi}_B(q)$ *are the Fourier transforms of the microscopic concentration operators,*

$$\hat{\phi}_A(\mathbf{q}) = \frac{1}{\rho_0}\sum_{\alpha=1}^{n}\sum_{i=\{A\}} \exp(\mathbf{q}\mathbf{r}_i^\alpha)$$
$$\hat{\phi}_B(\mathbf{q}) = \frac{1}{\rho_0}\sum_{\alpha=1}^{n}\sum_{i=\{B\}} \exp(\mathbf{q}\mathbf{r}_i^\alpha) \tag{42}$$

This part of the Hamiltonian leads to a microphase separation of copolymer melts, provided that $w_{AA} + w_{BB} - 2w_{AB} = -2k_B T\chi < 0$. Here χ is the usual Flory-Huggins parameter. The origin of interaction parameters w_{AA}, w_{BB}, w_{AB} is the van der Waals attraction between the monomers and the steric repulsive forces.

A mesoscopic description is introduced by defining functions $\phi_A(\mathbf{q})$ and $\phi_B(\mathbf{q})$ that have the meaning of the values of the microscopic concentration operators averaged over a mesoscopic volume. The conditional partition function, $Z(\phi_\gamma)$ ($\gamma = A, B$), is the partition function for the system subject to the constraint that the microscopic operators $\hat{\phi}_\gamma(\mathbf{q})$ ($\gamma = A, B$) are fixed at some prescribed values [42] of $\phi_\gamma(\mathbf{q})$, *i.e.*,

$$Z(\phi_\gamma) = N_0 \prod_{\alpha=1}^{n}\int D\mathbf{r}^\alpha W(\mathbf{r}^\alpha) \prod_{\gamma=A,B}\delta[\phi_\gamma(\mathbf{q}) - \hat{\phi}_\gamma(\mathbf{q})]\exp\left(-\frac{H_I}{k_B T}\right) \tag{43}$$

Here N_0 *is a constant,* Dr^α *denotes the measure* $(1/V)dr_0^\alpha\, dr_1^\alpha \ldots dr_N^\alpha$, *the interaction Hamiltonian* H_I *is given by Eq. (41), and* $W(r^\alpha)$ *is the distribution function, Eq. (40).*

For infinitely small χ there is no interaction in the system and the chains are mixed uniformly. The average values of $\phi_A(\mathbf{q})$ and $\phi_B(\mathbf{q})$ are equal to f and 1 - f, respectively. To describe the different phases in the system, we specify an order parameter $\Psi(\mathbf{r})$ as [2]

$$\Psi(\mathbf{r}) = \langle(1 - f)\,\phi_A(\mathbf{r}) - f\,\phi_B(\mathbf{r})\rangle \tag{44}$$

where $\langle\ldots\rangle$ denotes the thermal average. In the isotropic phase, $\Psi(\mathbf{r})$ is zero at every point and in the ordered phase it is nonzero. Assuming the system to be incompressible we have

$$\phi_A(\mathbf{r}) + \phi_B(\mathbf{r}) = 1 \tag{45}$$

then

$$\Psi(\mathbf{r}) = \langle\phi_A(\mathbf{r}) - f\rangle \tag{46}$$

The partition function, $Z(\phi_\gamma)$, cannot be calculated exactly. It could be rewritten by using the integral representation of the functional Dirac delta function and evaluated within the saddle place approximation. The calculations lead to the following expression [2, 43, 44]:

$$Z[\psi] = \exp\left\{-\sum_{n=2}^{\infty}\frac{1}{n!}\int\frac{d\mathbf{q}_1}{(2\pi)^3}\cdots\int\frac{d\mathbf{q}_n}{(2\pi)^3}\Gamma_n(\mathbf{q}_1,\ldots,\mathbf{q}_n)\cdot \delta(\mathbf{q}_1+\ldots+\mathbf{q}_n)\psi(-\mathbf{q}_1)\ldots\psi(-\mathbf{q}_n)\right\} \tag{47}$$

where *the vertex functions* Γ_n *for* $n > 2$ *are the well-known functions arising from the ideal chain conformations; the interaction Hamiltonian,* H_I, *is included only in* Γ_2.

In order to evaluate them [8] the discrete sums over set $\{A\}$ or $\{B\}$ in Eqs. (42) should be replaced by the integrals along the chains with the monomer distribution function $g(x)$ or 1 - $g(x)$, *i.e.*,

$$\sum_{i=\{A\}}\ldots \to N\int_0^1 \ldots g(x)dx \tag{48}$$

$$\sum_{j=\{B\}}\ldots \to N\int_0^1 \ldots [1-g(x)]dx \tag{49}$$

The monomer distribution function $g(x)$ gives the probability of finding a monomer of type A at distance $x \cdot N$ from the beginning of the chain. It should satisfy the following conditions: $0 < g(x) < 1$ for every x. Thus, a common diblock copolymer molecule is specified by

the step-like distribution function: $g(x) = \theta(x - f)$. The composition, f, can be expressed as

$$f = \int_0^1 g(x)dx \tag{50}$$

The full partition function is defined as

$$Z = \int D\psi Z[\psi] \tag{51}$$

but the Landau—Ginzburg free energy $F[\Psi]$ within the mean-field approximation (neglecting fluctuations) is simply

$$F[\Psi] = -k_B T \ln Z[\Psi] \tag{52}$$

In order to calculate the phase properties of the melt, that expansion is cut off at some lower order. The order parameter $\Psi(\mathbf{r})$ in the ordered phase which is characterized by the set $\{Q_{k,m}\}$ of the wave-vectors in the reciprocal space can be expanded as

$$\psi(\mathbf{r}) = \sum_{m=1}^{\infty} \frac{1}{\sqrt{n_m}} A_m \sum_{k=1}^{n_m} [\exp[i(\mathbf{Q}_{k,m}\mathbf{r} + \phi_{k,m})] + cc] \tag{53}$$

where *A_m and $\phi_{k,m}$ are amplitudes and phases of this expansion in the ordered phase; m numbers the shells and n_m is the number of wave-vectors in the mth shell.*

Their equilibrium values are determined by minimization of the free energy, $F[\Psi(\mathbf{r})]$, with respect to A_m and $\phi_{k,m}$ with additional constraints imposed on $\phi_{k,m}$ by the symmetry group of the ordered phase. The ordered phase with the smallest free energy for a given χN is the stable phase.

The phase diagram of the tapered copolymer melt computed within the two shell approximation [8] is shown in Fig. 15. The distribution function of monomer A along the tapered copolymer chains is

$$g(x) = \frac{1}{2}(1 - \tanh(c_1\pi(x - f_0)) \tag{54}$$

where *c_1 and f_0 determine the sharpness and the position of the "interface" between the blocks of A and B monomers.*

The distribution function $g(x)$ is shown in the insert of Fig. 15 for $c_1 = 3$, $f_0 = 0.5$ (solid line) and $f_0 = 0.3$ (dashed line). In the limit $c_1 \to \infty$, the diblock architecture is recovered. Changing f_0 can shift the position at which $g(x) = 0.5$ and the asymmetric model melts. In this case the melt composition $f = f_0$.

The Euler characteristic of the ordered phases can be computed as follows. At a given point of the phase diagram the equilibrium structure is characterized by the set of wave-vectors $Q_{k,m}$, phase $\phi_{k,m}$ and amplitudes A_n, the latter obtained by minimization. The order parameter distribution can be generated on a lattice by using Eq. (53). It is convenient to choose the lattice size as an integer number of main harmonics of the ordered structure, $2\pi/\mathbf{q}^*$, where $\mathbf{q}^*$ denotes the absolute maximum position in the scattering intensity. The Euler characteristic is then computed by using one of the algorithms described above.

The phase diagram 15 can be analyzed by using the Euler characteristics. The disordered phase contains no surface and, therefore, the Euler characteristic is zero. The *bcc* phase (Fig. 2d) within the two-shell approximation is expressed as

$$\psi_{BCC}(x,y,z) = A_1\left[\cos\frac{x}{\sqrt{2}}\cos\frac{y}{\sqrt{2}} + \cos\frac{y}{\sqrt{2}}\cos\frac{z}{\sqrt{2}} + \cos\frac{z}{\sqrt{2}}\cos\frac{z}{\sqrt{2}}\right] + A_2[\cos(\sqrt{2}x) + \cos(\sqrt{2}y) + \cos(\sqrt{2}z)] \tag{55}$$

where *amplitudes A_1 and A_2 are determined by minimizing Eq. (52) (e.g., $A_1 = 0.0345$, $A_2 = 0.00304$).*

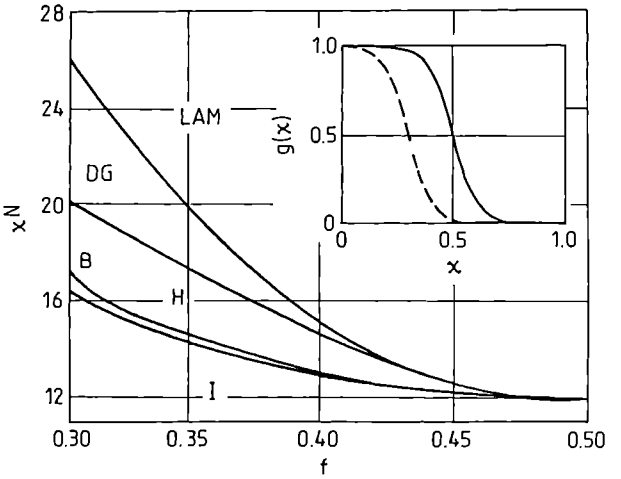

Fig. 15. The phase diagram of the gradient copolymer melt with the distribution functions $g(x) = (1/2)(1 - \tanh(c_1\pi(x - f_0))$ shown in the insert for $c_1 = 3$, $f_0 = 0.5$ (solid line) and $f_0 = 0.3$ (dashed line); x_i gives the position of ith monomer from the end of the chain in the units of the linear chain length; χ is the Flory-Huggins interaction parameter, N is the polymerization index, f is the composition ($f = \int_0^1 g(x)dx$). The Euler characteristic of the isotropic phase (I) is zero, hexagonal (H) — zero, for the BCC phase (B) $\chi_{Euler} = 4$ per unit cell, for the double gyroid phase (DG) $\chi_{Euler} = -16$ per unit cell, and for the lamellar phase (LAM) $\chi_{Euler} = 0$

Choosing the lattice size to be a period of the main harmonic, *i.e.*, $x = 2\pi\sqrt{2}\,\frac{i - 0.5N}{N}$, $i = 1, \ldots, N$ (N is the lattice size), we found the Euler characteristic of the *bcc* in the unit cell to be +4. This means that the ordered phase comprises two disconnected surfaces per unit cell, which is exactly the definition of the spherical mesophase of the *bcc* symmetry. Let us note that the form of the basis functions in Eq. (55) does not automatically guarantee the spherical morphology of the ordered phase. Thus when $A_1 \neq 0$ and $A_2 = 0$, $\chi_{Euler} = -12$, and when $A_1 = 0$ and $A_2 \neq 0$, $\chi_{Euler} = -32$ (eight minimal P surfaces [25] in unit cell).

The Euler characteristic of the hexagonal phase (Fig. 2c) is 0, since the Euler characteristic of each cylinder is zero. The double gyroid phase (Fig. 2b) within the two-shell approximation is represented as

$$\psi_{DG}(x,y,z) = A_1\left[\cos\frac{x}{\sqrt{6}}\sin\frac{y}{\sqrt{6}}\sin\frac{2z}{\sqrt{6}} + \right.$$
$$\left. + \cos\frac{y}{\sqrt{6}}\sin\frac{z}{\sqrt{6}}\sin\frac{2x}{\sqrt{6}} + \cos\frac{z}{\sqrt{6}}\sin\frac{x}{\sqrt{6}}\sin\frac{2y}{\sqrt{6}}\right] + \quad (56)$$
$$+A_2\left[\cos\frac{2x}{\sqrt{6}}\cos\frac{2y}{\sqrt{6}} + \cos\frac{2x}{\sqrt{6}}\cos\frac{2z}{\sqrt{6}} + \cos\frac{2y}{\sqrt{6}}\cos\frac{2z}{\sqrt{6}}\right]$$

The amplitude values are determined by minimizing Eq. (52) (*e.g.*, $A_1 = 0.152$, $A_2 = -0.038$). The Euler characteristic of the DG phase is -16 per unit cell (-8 for each G surface). Similarly to the *bcc* phase, the first two basis functions of the Ia$\bar{3}$d symmetry group do not automatically guarantee the DG morphology. For example, if amplitudes A_1 and A_2 are taken to be of the same sign, the S1 periodic surface of the Euler characteristics -52 is obtained [8]. Finally, the Euler characteristic of the lamellar phase (Fig. 2a) is again zero, since the Euler characteristic of a flat layer is 0. The volume fraction of the minority phase gradually increases as the *bcc* phase ($f_m = 0.352$) is transformed into the hexagonal ($f_m = 0.401$), double gyroid ($f_m = 0.43$) and, finally, into the lamellar phase ($f_m = 0.5$). The minority phase volume fraction of the BCC, HEX, DG and LAM phases depends weakly on the average composition f and on the Flory—Huggins parameter χ. This may be explained by a very scarce number of basic functions used to represent the symmetry groups considered.

At highly asymmetric compositions, the free-energy difference between the double-gyroid and the HPL phases becomes very small. Therefore, the HPL phase could be observed experimentally. In this case, as the temperature is decreased, the resulting phase transformations include I-BCC-HEX-HPL-HML-LAM. The HPL phase is represented within the two-shell approximation as

$$\Phi_{HPL}(x,y,z) = A_1\left[\cos(x) + \cos\frac{x-\sqrt{3}y}{2} + \cos\frac{x+\sqrt{3}y}{2}\right] + \quad (57)$$
$$+A_2\cos(dz)$$

where *d specifies the relative period of the lamellar ordering (compared to hexagonal).*

To calculate the Euler characteristic, we took the amplitudes A_1 and A_2 obtained by minimization of Eq. (52) (HPL phase is still metastable). There are two types of the HPL structures that can be modeled by using Eq. (57). The first structure (Fig. 16a) is bicontinuous, the Euler characteristics in a unit hexagonal cell is -8 (*e.g.*, at $A_1 = 0.154$, $A_2 = 0.17$). The two hexagonal sub-lattices of channels interpenetrate the lamellae, thus, in a unit cell, there is one big passage filled with the majority component and surrounded by 6 smaller passages filled with the minority component (only a half of each small channel is in a unit cell). In the second structure (Fig. 16b), the alternating stack of lamellae is penetrated by hexagonally arranged columns that are rich in one of the components (phase volume fractions are nearly symmetric), thus the structure is only mono-continuous (the true catenoid phase). In the latter case the Euler characteristic is -2, *i.e.*, one passage is per one unit hexagonal cell (*e.g.*, at $A_1 = 0.154$, $A_2 = 0.3$).

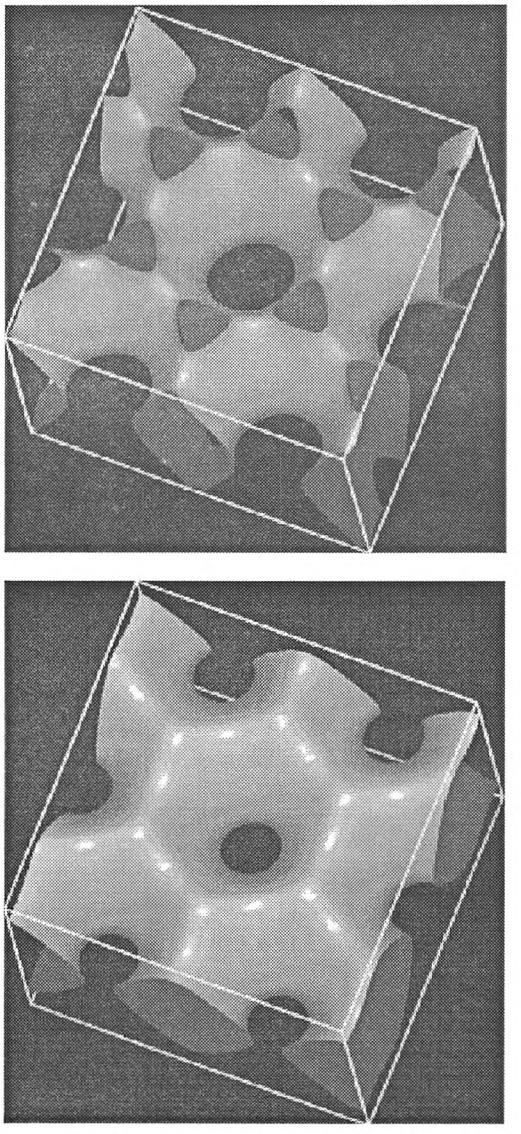

Fig. 16. The bicontinuous (a) and the mono-continuous (b) HPL structures

The Euler characteristics density of the bicontinuous HPL structure is close to the Euler characteristics density of the DG phase. Also, the free-energy cost of the bicontinuous HPL phase is similar to the cost of the DG phase. Since there are small topological and free-energy barriers, these structures could be easily intertransformed by applying external fields. Their phase volume fractions are also similar ($f_m^{DG} = 0.43$, $f_m^{HPL_1} = 0.46$). The second (mono-continuous) type of the HPL structure is topologically and energetically close to the lamellar (or HML) phase.

The universal character of the bicontinuous-to-droplets transformation

The transformation of the bicontinuous morphology into the disperse droplet pattern is seen to occur in

many mesoscopic systems. For example, in the asymmetric diblock copolymer melt, the interconnected structures such as a double gyroid phase can be transformed into the disperse spherical morphology (of the BCC or CPS symmetries) by increasing the temperature. The pathway of such a transformation involves the formation of cylindrical morphology at the intermediate stage [45]. Similarly, the sponge phase in the surfactant solutions is transformed into the micelle phase *via* some cylindrical mesophases [46]. During the phase separation process, the morphology of the asymmetric binary mixture could be either bicontinuous or disperse, and, at some quench conditions (when the final equilibrium minority phase volume fraction is slightly below the percolation threshold), this transformation takes place dynamically. The pathway of such transformations can be investigated by analyzing the domain sizes and shapes in the vicinity to the percolation transition $\chi_{Euler} \approx 0$.

In order to find correlations between the shapes and sizes of the domains, the droplet surface area density, S, was plotted as a function of droplet compactness, C, for each droplet detected in the system at four time steps of the simulation, Fig. 17a. The droplet compactness has been defined as

$$C = 6\pi V/S^{3/2} \tag{58}$$

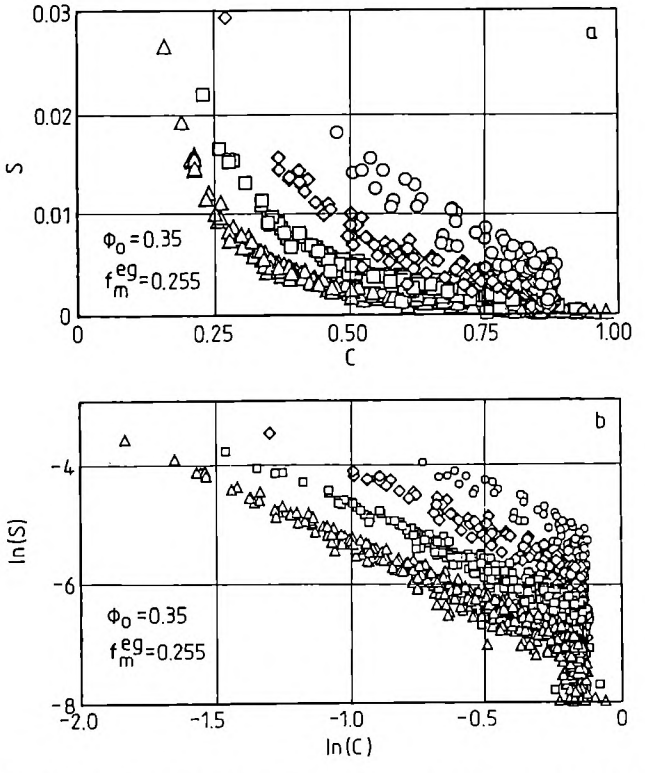

Fig. 17. a) The droplet surface area density, S, as a function of droplet compactness, $C = 6\pi V/S^{3/2}$, plotted for each droplet detected in the system at the four time steps of the spinodal decomposition of the asymmetric mixture. b) The parabolic slopes of these dependencies, indicate the decomposition of cylindrical droplets illustrated in Figure 18

where *S is the droplet surface area and V is the droplet volume.*

The droplets of low compactness have sizes bigger than average. When the transformation from bicontinuous to disperse morphology is slow, the power law type relation ships can be observed between the droplet size and compactness in the low compactness limit. A double-logarithmic plot of these relations ships (Fig. 17b) reveals that they are parabolic (the slopes in the low compactness limit are -2 ± 0.1). Consider now a cylindrical (highly elongated) domain of length l and cross section radius R (Fig. 18). The area of such a domain is $S \approx 2\pi Rl$, and its compactness $c \approx \frac{3}{\sqrt{2}} \cdot \sqrt{R/l}$. Now, if we keep the cross section radius R constant and increase

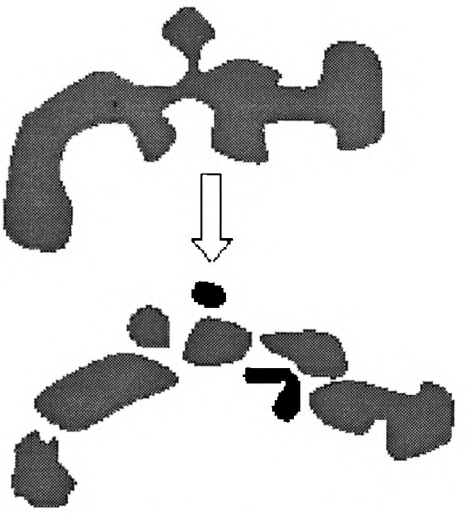

Fig. 18. Schematic illustration of the cylinder-droplets transformation (see also Fig. 17)

the length of the domain l, the domain area would increase as its compactness decreases: $S(l) \sim C(l)^{-2}$. That is exactly what is shown in Fig. 17: the droplets area are formed on account of the decomposition of the highly elongated (cylindrical) domains (see also Fig. 18). Thus, also during the phase separation, the transformation from bicontinuous to droplet pattern involves the formation of cylindrical domains, which suggests that it is a universal feature of such transformations.

CONCLUDING REMARKS

The results presented above are restricted to the class of binary systems well described by the simple Landau-Ginzburg or Flory-Huggins free-energies. In more complex systems, some morphological features could be significantly different (*e.g.*, the percolation threshold value). However, the methods used here to characterize the morphological transformations are not limited to

any specific class of the systems and can be used to study any other dynamic or equilibrium phenomena. We hope that this present study will stimulate applications of quantitative morphological methods in the physics and chemistry of polymers.

REFERENCES

1. Bray A. J.: *Adv. Physics* 1994, **43**, 357.
2. Leibler L.: *Macromolecules* 1980, **13**, 1602.
3. Fredrickson G. H., Helfand E.: *J. Chem. Phys.* 1987, **87**, 697.
4. Matsen M. W., Schick M.: *Phys. Rev. Lett.* 2000, **72**, 2660.
5. Matsen M. W., Schick M.: *Macromolecules* 1994, **27**, 4014.
6. Matsen M. W., Schick M.: *Curr. Opin. Coll. Int. Sci.* 1996, **1**, 329.
7. Matsen M. W., Bates F. S.: *Macromolecules* 1996, **29**, 1091.
8. Aksimentiev A., Hołyst R.: *J. Chem. Phys.* 1999, **111**, 2329.
9. Molau G. E.: "Block Copolymers" (Ed., Aggarawal S. L.), Planum Press, New York 1970.
10. Thomas E. L. *et al.*: *Macromolecules* 1986, **19**, 2197.
11. Herman D. S. *et al.*: *Macromolecules* 1987, **20**, 2940.
12. Hasegawa H. *et al.*: *Macromolecules* 1987, **20**, 1615.
13. Thomas E. L. *et al.*: *Nature* 1988, **334**, 598.
14. Hajduk D. A., Harper P. E., Gruner S. M., Honeker C. C., Kim G., Thomas E. L., Fetters L. J.: *Macromolecules* 1995, **28**, 2570.
15. Mogi Y. *et al.*: *Macromolecules* 1992, **25**, 5408.
16. Stadler R. *et al.*: *Macromolecules* 1995, **28**, 3080.
17. Verhoogt H., van Dam J., Posthuma de Boer A., Draaijer A., Houpt P. M.: *Polymer* 1993, **34**, 1325.
18. Jinnai H., Koga T., Nishikawa Y., Hoshimoto T., Hyde S. T.: *Phys. Rev. Lett.* 1997, **78**, 2248.
19. Jinnai H. *et al.*: *Phys. Rev. Lett.* 2000, **84**, 518.
20. Jinnai H., Nishikawa Y., Hashimoto T.: *Phys. Rev. E* 1999, **59**, R2554.
21. Mecke K. R.: *International Journal of Modern Physics B* 1998, **12**, 861.
22. Sofonea V., Mecke K. R.: *Eur. Phys. J. B* 1999, **8**, 99.
23. Nishikawa Y., Jinnai H., Koga T., Hashimoto T., Hyde S. T.: *Langmuir* 1998, **14**, 1242.
24. Hilbert D.: "Geometry and the Imagination", Chelsea Publishers, New York 1952.
25. Góźdź W., Holyst R.: *Phys. Rev. E* 1996, **54**, 5012.
26. Holyst R., Góźdź W.: *J. Chem. Phys.* 1997, **106**, 4773.
27. Hoffman D. A.: *J. Phys. (Paris) Coloq.* 1990, **51**, c7—197.
28. Lorensen W. E., Cline H. E.: *Computer Graphics* 1987, **21**, 163.
29. Aksimentiev A., Biben T., Holyst R., Moorthi K.: Jap. Pat. Appln. No. 2000-221562.
30. Doi A., Koide A.: *IEICE Transformations Commun., Elec. Info. Syst.* 1991, **E74(1)**, 214.
31. Gueziec A., Hummel R.: *IFEE Transactions on Visualization and Computer Graphics* 1995, **1(4)**, 328.
32. Pincus P.: *J. Chem. Phys.* 1981, **75**, 1996.
33. Koga T., Kawasaki K.: *Physica A* 1993, **196**, 389.
34. de Gennes P. G.: *J. Chem. Phys.* 1980, **72**, 4756.
35. Binder K.: *J. Chem. Phys.* 1983, **79**, 6387.
36. Puri S., Oono Y.: *Phys. Rev. A* 1988, **38**, 1542.
37. van Vlimmeren B. A. C., Fraaije J. G. E. M.: *Comput. Phys. Commun.* 1996, **99**, 21.
38. van Kampen N. G.: "Stochastic Processes in Physics and Chemistry", Elsevier Science 1992.
39. Aksimentiev A., Moorthi K., Holyst R.: *J. Chem. Phys.* 2000, **112**, 6049.
40. Ohta T., Kawasaki K.: *Macromolecules* 1986, **19**, 2621.
41. Edwards S. F.: *Proc. Phys. Soc. (London)* 1996, **88**, 265.
42. Landau L. D., Lifshitz E. M.: "Statistical Physics, Part 1", 3rd edition, Pergamon Press, Oxford 1980, p. 479.
43. Holyst R., Vilgis T. A.: *Macromol. Theory Simul.* 1996, **5**, 573.
44. Aksimentiev A., Holyst R.: *Macromol. Theory Simul.* 1999, **8**, 328.
45. Kimishima K., Koga T., Hashimoto T.: *Macromolecules* 2000, **33**, 968.
46. Tlusty T., Safran S. A., Strey R.: *Phys. Rev. Lett.* 2000, **84**, 1244.